remote sensing

MDPI

Article

Advection of Biomass Burning Aerosols towards the Southern Hemispheric Mid-Latitude Station of Punta Arenas as Observed with Multiwavelength Polarization Raman Lidar

Athena Augusta Floutsi [1,*], Holger Baars [1], Martin Radenz [1], Moritz Haarig [1], Zhenping Yin [1,2,3], Patric Seifert [1], Cristofer Jimenez [1], Albert Ansmann [1], Ronny Engelmann [1], Boris Barja [4], Felix Zamorano [4] and Ulla Wandinger [1]

[1] Leibniz Institute for Tropospheric Research, 04318 Leipzig, Germany; baars@tropos.de (H.B.); radenz@tropos.de (M.R.); haarig@tropos.de (M.H.); ZP.Yin@whu.edu.cn (Z.Y.); seifert@tropos.de (P.S.); jimenez@tropos.de (C.J.); albert@tropos.de (A.A.); ronny@tropos.de (R.E.); ulla@tropos.de (U.W.)
[2] School of Electronic Information, Wuhan University, Wuhan 430072, China
[3] Key Laboratory of Geospace Environment and Geodesy, Ministry of Education, Wuhan 430079, China
[4] Atmospheric Research Laboratory, University of Magallanes, Punta Arenas 621-0427, Chile; boris.barja@umag.cl (B.B.); felix.zamorano@umag.cl (F.Z.)
* Correspondence: floutsi@tropos.de

Abstract: In this paper, we present long-term observations of the multiwavelength Raman lidar Polly^{XT} conducted in the framework of the DACAPO-PESO campaign. Regardless of the relatively clean atmosphere in the southern mid-latitude oceans region, we regularly observed events of long-range transported smoke, originating either from regional sources in South America or from Australia. Two case studies will be discussed, both identified as smoke events that occurred on 5 February 2019 and 11 March 2019. For the first case considered, the lofted smoke layer was located at an altitude between 1.0 and 4.2 km, and apart from the predominance of smoke particles, particle linear depolarization values indicated the presence of dust particles. Mean lidar ratio values at 355 and 532 nm were 49 $\pm$ 12 and 24 $\pm$ 18 sr respectively, while the mean particle linear depolarization was 7.6 $\pm$ 3.6% at 532 nm. The advection of smoke and dust particles above Punta Arenas affected significantly the available cloud condensation nuclei (CCN) and ice nucleating particles (INP) in the lower troposphere, and effectively triggered the ice crystal formation processes. Regarding the second case, the thin smoke layers were observed at altitudes 5.5–7.0, 9.0 and 11.0 km. The particle linear depolarization ratio at 532 nm increased rapidly with height, starting from 2% for the lowest two layers and increasing up to 9.5% for the highest layer, indicating the possible presence of non-spherical coated soot aggregates. INP activation was effectively facilitated. The long-term analysis of the one year of observations showed that tropospheric smoke advection over Punta Arenas occurred 16 times (lasting from 1 to 17 h), regularly distributed over the period and with high potential to influence cloud formation in the otherwise pristine environment of the region.

Keywords: biomass burning aerosols; tropospheric aerosol; Raman lidar; Punta Arenas; DACAPO-PESO

Citation: Floutsi, A.A.; Baars, H.; Radenz, M.; Haarig, M.; Yin, Z.; Seifert, P.; Jimenez, C.; Ansmann, A.; Engelmann, R.; Barja, B.; et al. Advection of Biomass Burning Aerosols towards the Southern Hemispheric Mid-Latitude Station of Punta Arenas as Observed with Multiwavelength Polarization Raman Lidar. *Remote Sens.* **2021**, *13*, 138. https://doi.org/10.3390/rs13010138

Received: 30 November 2020
Accepted: 1 January 2021
Published: 4 January 2021

1. Introduction

Punta Arenas (53.2°S, 70.9°W) is located at the Strait of Magellan, at the southern tip of South America (location indicated with yellow star in Figure 1). Constant westerly to northwesterly winds prevail through the whole year induced by the Antarctic low-pressure belt [1]. Since it is located in the most southerly continental area (with the exception of Antarctica), with New Zealand, Tasmania and Australia being the nearest (roughly 8.000 km) landmasses towards the direction of the prevailing winds, clean, pristine marine air masses dominate the aerosol conditions. The aforementioned geographical and climatic

conditions make Punta Arenas an ideal test-bed for studies of aerosol, aerosol–cloud and radiation interactions under rather clean conditions with low anthropogenic impact [2–4].

In the southern mid-latitudes, there is a lack of long-term ground-based remote-sensing observations of aerosols and clouds, mainly due to the absence of substantial land masses below 40 degrees latitude. Immler and Schrems [5] used the pristine location of Punta Arenas to contrast the properties of mid-latitude cirrus clouds from those observed in the aerosol-burden northern midlatitudes. The first lidar-based studies of the vertical aerosol distribution over Punta Arenas have been performed by the "Aerosol Lidar Measurement at Punta Arenas in the Frame of Chilean–German Cooperation" (ALPACA) campaign [4,6,7]. The portable Raman lidar Polly^{XT} [8,9] was deployed at the Magallanes University in Punta Arenas and operated continuously for 4 months (4 December 2009–4 April 2010). During the ALPACA campaign, pristine marine conditions dominated the measurements, while lofted aerosol layers were observed only eight times. From these eight lofted layers examined, seven of them had an aerosol optical depth (AOD) of less than 0.05. The origins of these layers were mainly bush fires in Australia and Patagonian dust [4].

As a follow-up of ALPACA, the Dynamics, Aerosol, Cloud and Precipitation Observations in the Pristine Environment of the Southern Ocean (DACAPO-PESO) campaign started in November 2018 as a collaboration between the Leibniz Institute for Tropospheric Research (TROPOS), the Leipzig Institute for Meteorology (LIM) and the University of Magallanes (UMAG) in Punta Arenas, Chile. DACAPO-PESO is focused on the investigation of cloud formation and aerosol–cloud interactions in environments of contrasting aerosol conditions, and relies mainly on synergistic algorithms using state-of-the-art lidar and radar techniques. More information on the campaign and instrumentation is given in Section 2.

During two years of continuous measurements in the framework of DACAPO-PESO, clean marine aerosol conditions dominated the atmosphere above Punta Arenas. However, there were several cases in which the aerosol burden was high in both the troposphere and the stratosphere. The massive bushfires of southeastern Australia in the summer season of 2019–2020 injected enormous amounts of smoke into the upper and lower stratosphere, which were then transported by the prevailing westerly winds to South America within 1–2 weeks. During January 2020, we observed these stratospheric smoke layers with our lidar system over Punta Arenas at heights of 25–30 km (AOD reached values up to 0.85 at 532 nm). For a more detailed description of this event, with a specific focus on the stratospheric smoke optical properties, readers should refer to Ohneiser et al. [10].

Within this publication, we focus on the tropospheric aerosol layers that were advected over Punta Arenas. In order to demonstrate the tropospheric conditions in this clean and pristine environment under such events, lidar observations of the vertical distribution of two distinctively different lofted layers (in terms of physical and optical properties) are presented in detail. In addition, since aerosol particles influence the evolutions, lifetimes and microphysical properties of clouds by acting as cloud condensation nuclei (CCN) and ice nucleating particles (INP), CCN and INP concentrations were derived from the lidar signals for the corresponding cases.

This paper is organized as follows: Section 2 provides information on the experiment, data sources, instrumentation and methodology. Section 3 presents our analysis for two different smoke events as observed over the site of Punta Arenas, focusing on the optical properties of the aerosol particles. An overview of all the lofted layers that were observed, above our measurement site, during 2019 is also presented. Section 4 discusses the main findings and highlights the most important conclusions of this study.

2. Experiment, Instrumentation and Methodology

The DACAPO-PESO (https://dacapo.tropos.de/) campaign started in November 2018 and will continue until the end of 2020. This campaign is focused on aerosol, clouds, ice nucleation particles and aerosol–cloud dynamics relationships in the pristine environ-

ment of the Southern Hemisphere midlatitudes. These complex topics need a synergistic approach in terms of instrumentation, and therefore the Leipzig Aerosol and Cloud Remote Observations System (LACROS, [11]) was deployed on site (53.2°S, 70.9°W, 9 m above sea level, a.s.l.). LACROS comprises a unique set of active and passive remote-sensing instruments which are to a large extent containerized (Figure 1). More specifically, some key components are a 35 GHz cloud radar, a Raman and depolarization lidar as part of PollyNET [7], a 2-µm scanning Doppler lidar, a 24-GHz micro rain radar, a microwave radiometer, a Sun photometer, a disdrometer and a radiation station with an all-sky camera. In addition, a 94-GHz cloud radar (provided by LIM) was also deployed until 1 October 2019. A Sun photometer was installed on the roof platform of the main building of UMAG, as part of the Aerosol Robotic Network (AERONET, [12]). The LACROS observations are accompanied by regular observations of a multi-wavelength lidar of UMAG, which is operated at the site since 2016 in the frame of the South American Environmental Risk Management Network (SAVER-Net) and the Latin-American Lidar Network (LALINET) [13].

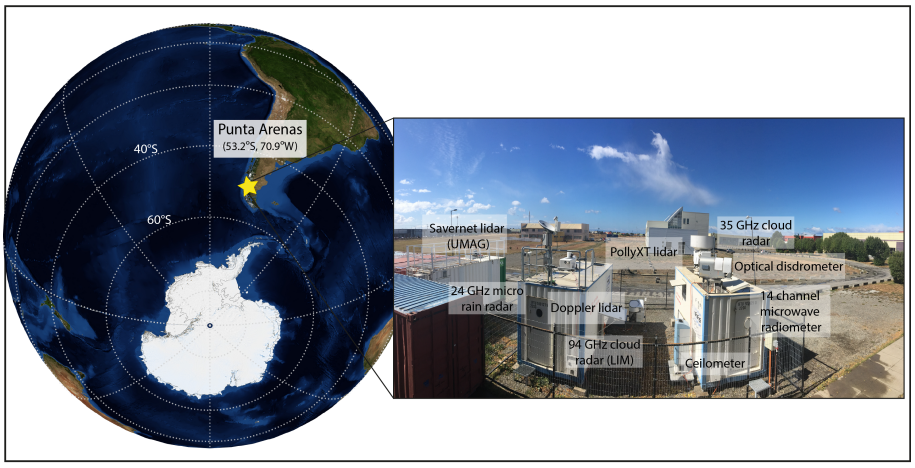

Figure 1. Map of the location of Punta Arenas (indicated by a yellow star) in Chile, South America. The LACROS observational facility, as deployed at UMAG, can be seen on the right side.

2.1. Lidar Measurements

In this paper, we will focus on atmospheric measurements which were conducted with the Raman lidar Polly^{XT} [7,9]. Polly^{XT} utilizes a Nd:YAG laser that emits light at 3 different wavelengths, which are 355, 532 and 1064 nm at energies of 60, 110 and 180 mJ respectively. The receiver consists of 12 channels and enables measurements of elastically (355, 532, 1064 nm), and Raman scattered light (387, 607 nm for aerosols and 407 nm for water vapour), and depolarization state of the backscatter light (at 355 and 532 nm). A near-range telescope allows the detection of 355, 387, 532 and 607 nm scatter light from about 60–80 m above ground. Vertical profiles can be obtained with an uppermost detection height of around 20 km a.g.l. (above ground level). Data from all channels are acquired with a vertical resolution of 7.5 m and a temporal resolution of 30 s.

With this setup, the backscatter coefficient at 355, 532 and 1064 nm and the extinction coefficient at 355 and 532 nm can be determined as described by Ansmann and Müller [14]. Typically, uncertainties for the Raman retrieved backscatter and extinction coefficient are in the range of 5–10% and 10–20%, respectively [8,9,15]. From these extensive optical properties, the so-called intensive optical properties (i.e., type dependent), such as lidar ratio and Ångström exponent, can be determined and used for aerosol characterization [16]. Another intensive optical property, the linear depolarization ratio, is defined as the cross-polarized-to-co-polarized backscatter ration (orthogonal and parallel planes of polarization to the plane of linear polarization of the transmitted laser pulses, respectively) and was determined according to standard procedures applied in the European lidar network EARLINET [17,18]. Data are quality assured, since quality assurance (QA) procedures are

a key aspects within the EARLINET network (e.g., [19–21]) and are followed even when Polly lidar systems are operated outside Europe.

The lidar signal returns were vertically smoothed with a gliding average filter, in order to reduce the influence of noise. Window lengths varied for the two cases considered (Sections 3.1 and 3.2), according to the solar background noise depending on daytime and season, and the vertical structure of the aerosol layers of interest. For the first case study, a window length of 562.5 m was applied for the backscatter coefficient, Ångström exponent and particle linear depolarization ratio, while a window length of 1492.5 m was applied for the much noisier Raman-retrieved extinction and thus also the lidar ratio. For the second case, a window length of 307.5 m was used for the backscatter coefficient and the particle linear depolarization ratio profiles, and a length of 1492.5 m was applied to the Ångström exponent.

The retrieval of CCN and INP is based on the method developed by Mamouri and Ansmann [22]. At this point, a short summary is provided for the reader.

All particles with a radius larger than a certain threshold (50 nm for smoke ($n_{50,s}$), 100 nm for mineral dust ($n_{100,d}$)) are assumed to activate as CCN at supersaturation of 0.2%. To calculate the INP the surface area concentration is needed (e.g., [23]).

Long-term Aeronet observations of the particle size distribution are used to derive conversion factors $c_{50,s}$, $c_{100,d}$ and χ_i from extinction coefficient (measurable with lidar) to particle number concentration and surface area concentration (s_i). These conversion factors are aerosol type specific (index i for smoke (s) and dust (d)). The contributions of different aerosol types to the particle backscatter coefficient are determined using the particle linear depolarization ratio (e.g., [22,24]). To obtain the extinction coefficient σ_i, lidar ratios of 65 sr and 50 sr are applied to the smoke and dust backscatter coefficients, respectively. The number concentrations ($n_{50,s}$, $n_{100,d}$) and surface area concentration are derived with these relationships:

$$n_{50,i} = c_{50,i} \times \sigma_i^{\chi_i}$$

$$s_i = c_{s,i} \times \sigma_i$$

The conversion factors for aged smoke ($c_{50,s}$ = 28.2 cm^{-3}, χ_s = 0.71, $c_{s,s}$ = 1.73 × 10^{-12} Mm m^2 cm^{-3}) were derived from Aeronet stations in southern South America [25]. The dust conversion factors ($c_{100,d}$ = 7.71 cm^{-3}, χ_d = 0.73, $c_{s,d}$ = 2.39 × 10^{-12} Mm m^2 cm^{-3}) are derived from Aeronet stations in America/Australia [26].

2.2. Auxiliary Data

Lidar signal returns need to be corrected for Rayleigh scattering and thus auxiliary meteorological observations are needed. Rayleigh influences are corrected using Global Data Assimilation System 1 (GDAS1) temperature and pressure profiles with 1° horizontal resolution from the National Weather Service's National Centers for Environmental Prediction [27].

The Sun photometer located at UMAG (53.1°S, 70.9°W, 25 m a.s.l., site name: Punta_Arenas_UMAG), measures the column-integrated extinction coefficient at 8 channels from 340 to 1640 nm. Level 1.5 AOD data are used with a corresponding uncertainty of 0.01–0.02 [28] as level 2.0 data are not yet available.

For the analysis of the air mass transport the HYSPLIT model was used [29]. HYSPLIT model calculates backward and forward trajectories of air masses for simulations of dispersion and deposition at a given location. In order to identify the aerosol sources and to create some statistical basis of the aerosol conditions during DACAPO-PESO, we used ensemble backward trajectories combined with a land cover classification for a temporally and vertically resolved air mass source attribution TRACE [30,31]. A simplified version of the MODIS land cover [32] is used. As a first step, a 27-member ensemble of 10 day backward trajectories is calculated using HYSPLIT. Meteorological input data for HYSPLIT were downloaded GDAS1 (https://www.ready.noaa.gov/gdas1.php) provided by the Air Resources Laboratory (ARL) of the US National Weather Service's National Centers

for Environmental Prediction (NCEP). Each ensemble is generated using a small spatial offset in the trajectory endpoint. Whenever a trajectory is located below the planetary boundary layer (PBL) height provided by the GDAS1 data ("reception height"), the land cover is categorized using custom defined polygons according to land mass boundaries. It is therefore assumed that an air parcel is influenced by the surface type if the corresponding trajectory is below the PBL height. The residence time for each category is then the total time an air parcel fulfilled this criterion by land cover category. This calculation is repeated in steps of 3 h in time and 500 m in height in order to provide a continuous estimate on the source of the air mass and a first indication on the potential aerosol load.

3. Results and Discussion

In this section, two of the most distinctive cases of tropospheric lofted aerosol layers that were identified above Punta Arenas are presented in detail. The first one presents a 3 km thick lofted aerosol layer, located in the lowest troposphere between 1.0 and 4.2 km. Source attribution with TRACE indicated that the layer originated from Central and Central-South Chile, where wildfires occurred at the same time. The second case shows thin (geometrically and optically) aerosol layers, as observed by Polly^{XT}, at altitudes of 5.5–7.0, 9.0 and 11.0 km after a long-range transport event from Australia. The retrieved optical properties indicate that the layers consist of smoke particles. The retrieved optical parameters for the two case studies are summarized in Table 1. In addition, a long-term analysis of occurrence of lofted layers for 2019 is also presented.

Table 1. Overview of aerosol optical properties as derived from Polly^{XT} LACROS in Punta Arenas on 5 February 2019 and 11 March 2019. β is the backscatter coefficient, S the lidar ratio, δ the particle linear depolarization ratio and Å the backscatter-related Ångström exponent. The subscript indicates the corresponding wavelength. All values correspond to averaged (mean) values per examined layer along with the standard deviation.

Date	Alt. (km)	β_{355}, β_{532}, β_{1064} (Mm^{-1} sr^{-1})	S_{355}, S_{532} (sr)	δ_{532} (%)	Å$_{355/532}$, Å$_{532/1064}$
5 February 2019	1–4.2	0.90 ± 0.25	49 ± 12	7.6 ± 0.23	0.76 ± 0.23
		0.67 ± 0.23	24 ± 18		0.97 ± 0.29
		0.34 ± 0.11			
11 March 2019	11	-	-	8.3 ± 1.0	-
		0.20 ± 0.11	-	-	0.72 ± 0.04
		0.100 ± 0.05	-	-	-

3.1. Lofted Smoke Layers from South America

From 4 February to 5 February 2019, several lofted aerosol layers were observed between 1 and 4.5 km in height. Figure 2 shows a two-day overview of main lidar parameters, the Sun-photometer-derived AOD, atmospheric thermodynamics and a target classification [33] measured by Polly^{XT}. As indicated in Figure 2, a free-tropospheric aerosol plume with a geometrical thickness of 3 km was present on 4 February 2019 between 02:00 and 19:30 UTC. The target classification (Figure 2d) clearly identifies this aerosol up to about 4.3 km in height but was not able to identify the types of the aerosol particles present as a result of weak backscattering signals. The AOD during that day was low, with a mean value of 0.05 at the wavelength of 500 nm. From the beginning of the campaign until March 2019, the mean daily averaged aerosol optical thickness at Punta Arenas was found to be 0.03 (at 500 nm); thus, a slightly increased AOD was observed. The aforementioned layer was characterized by low depolarization ratio values that indicate the presence of spherical particles. From the Ångström exponent (Figure 2a), we can conclude that the layer consisted mainly of fine-mode aerosol particles (i.e., particles smaller than 1 µm).

The following day, on 5 February 2019, a descending aerosol layer was observed between 07:00 and 12:00 UTC (Figure 2b). The layer extented from 1.0 to 4.2 km in height. In contrast to the layer from the previous day, this one was characterized by

higher backscatter and a low to moderate depolarization ratio with the most pronounced features found between 1.6 and 2.8 km (Figure 2c). The higher values of volume linear depolarization ratio, with respect to the previous day, indicate the presence of non-spherical particles. Similarly to the previous day, the AOD during that event was low, with maximum and mean values of 0.09 and 0.05 respectively (at 500 nm, Figure 2a), the mean still being three times higher than the average. Around 18:00 UTC we observed the formation of a cloud, which according to the target classification (Figure 2d) consisted of ice crystals, thereby indicating that ice formation is most likely supported by the advection of the smoke particles acting as INP, as discussed below.

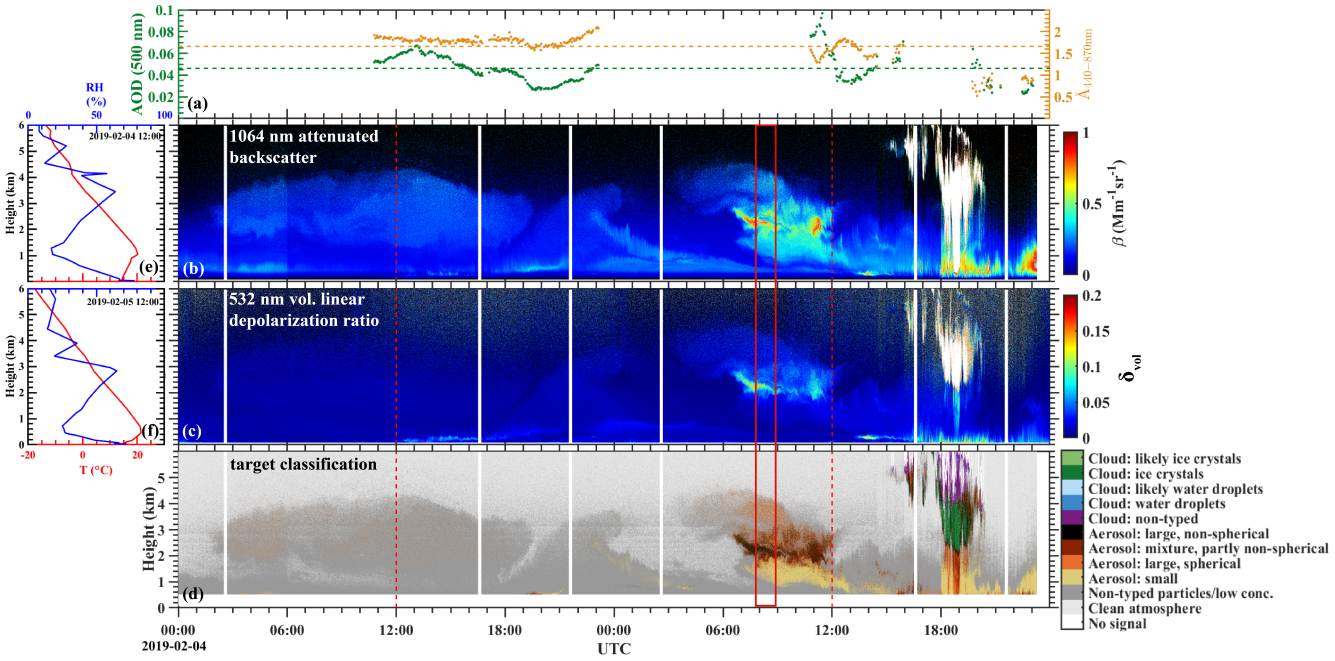

Figure 2. From the upper to the lower panel: (**a**) aerosol optical depth (AOD) at 500 nm and Ångström exponent for 440/870 nm (dashed lines indicate the mean); (**b**) attenuated backscatter coefficient at 1064 nm (Mm^{-1} sr^{-1}); (**c**) volume depolarization ratio (% at 532 mn); and (**d**) target classification reflecting the atmospheric conditions over Punta Arenas from 4 February to 5 February 2019. Radiosonde launches are depicted with red dashed lines. The corresponding temperature and relative humidity profiles can be seen on the left panels (**e**,**f**). Vertical white lines indicate the automatic calibration of the linear depolarization ratio (Engelmann et al. [9]). The averaging period for the profiles shown in Figure 5 is indicated by the red rectangul.

Further context of the air masses arriving at Punta Arenas is given by the HYSPLIT backward trajectory analysis shown in Figures 3 and 4. The 10-day backward trajectories presented in Figure 3 show that the vast majority of the air parcels arriving over Punta Arenas at 3000 m in height originated from the southern Pacific Ocean. Shortly (1–2 days) before the arrival of the air parcels to Punta Arenas, they passed over the regions of Central and Central-South Chile (Figures 3 and 4b). Figure 3c demonstrates that no precipitation occurred while the trajectories passed over the land masses. Air masses crossed above lands that were categorized as forest, savanna, grass and barren (Figure 4a) and belong to South America (Figure 4b). According to FIRMS (Fire Information for Resource Management System, not shown here), on the 2nd and 3rd of February 2019, when the air parcels were located above the aforementioned regions, active fires and wildfires occurred over the region passed by the trajectories. During the summer months (December to February), wildfires are common in Chile, especially between the regions of Valparaíso and Los Lagos, due to the extremely dry conditions and the prevailing westerlies. Relative humidity in the aerosol layer (Figures 2e,f and 3b) was mostly below 60%, and therefore we do not expect any hygroscopicity effects on the aerosol observed. As the air masses crossed above

active fire regions 1–2 days before they were observed by our system, the presence of partly coated soot particles was expected. Apart from smoke particles, soil dust is also thought to have been present in the observed layer due to turbulent fire-related winds that developed above the burning areas [34,35].

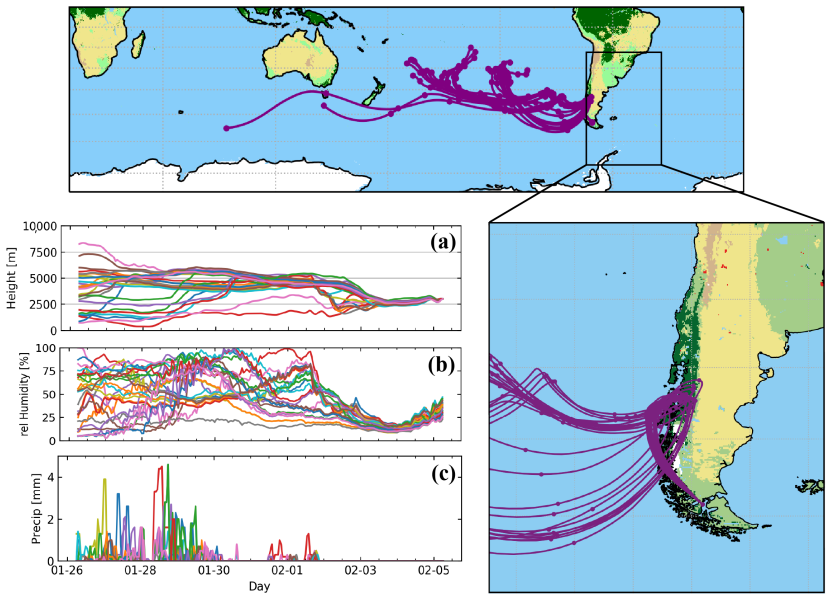

Figure 3. Top: the 10-day HYSPLIT backward trajectories ending at Punta Arenas, Chile, on 5 February 2019, 06:00 UTC, at 3 km altitude. (**a**) the altitudes (m) at which the air masses were traveling, (**b**) the relative humidities (%) of the air masses and (**c**) the precipitation in mm. Right: Zoom of top panel.

Figure 5 presents the optical properties profiles of the lofted aerosol layer observed in the troposphere above Punta Arenas in the morning of 5 February 2019. For the lowest 2.4 km, the backscatter coefficient (Figure 5a) exhibits a relatively strong spectral dependency, which is typical for smoke (mean values of 0.90 ± 0.25 Mm^{-1} sr^{-1}, 0.67 ± 0.23 Mm^{-1} sr^{-1} and 0.34 ± 0.11 Mm^{-1} sr^{-1} for 355, 532 and 1064 nm respectively). Within this layer, the extinction coefficient (not shown here) reached values up to 65 Mm^{-1} at 355 nm and 39 Mm^{-1} at 532 nm, exhibiting a weaker spectral dependency. Such extinction values are typical for tropospheric smoke layers, as previously reported in the literature [3,36,37]. Mean lidar ratio (Figure 5b) values were 49 ± 12 sr and 24 ± 18 sr for 355 and 532 nm, respectively. The lidar ratios reported here are consistent with previously published results [6,7,15,24,38–41]. However, it should be noted that differences in the burned vegetation type, location (e.g., Eastern Europe, Siberia or Canada), fire type (smoldering or flaming combustion) and the age of the smoke particles induce the relatively large range of values reported in the literature. The depolarization ratio of less than 5% (at 532 nm, Figure 5d) is also further supporting the presence of nearly spherical scatterers below 2 km [37]. Backscatter-related Ångström exponents of 0.76 ± 0.23 and 0.97 ± 0.29 at the wavelength pairs of 355/532 nm and 532/1064 nm, respectively, were determined by lidar observations (Figure 5c), and indicate the presence of coarse particles within the smoke layer. In comparison, Foth et al. [4] reported a backscatter-related Ångström exponent (532/1064 nm) of 0.56 ± 0.21 for a Patagonian dust layer and of 0.61 ± 0.1 for a smoke plume originating from Australia. Within the smoke plume, the linear particle depolarization ratio (Figure 5d) ranged from 2% to 14% (mean: 7.6 ± 3.6%) at 532 nm with the maximum being observed between 2.2 and 2.3 km. The slightly elevated particle linear depolarization ratio at this altitude can be explained by the presence of irregularly shaped soil dust particles [34], along with some partly coated soot particles. The smoke–dust

mixture was mostly confined between 2.0 and 2.8 km, and it was well identified by the target classification algorithm as a partly non-spherical mixture (Figure 2d).

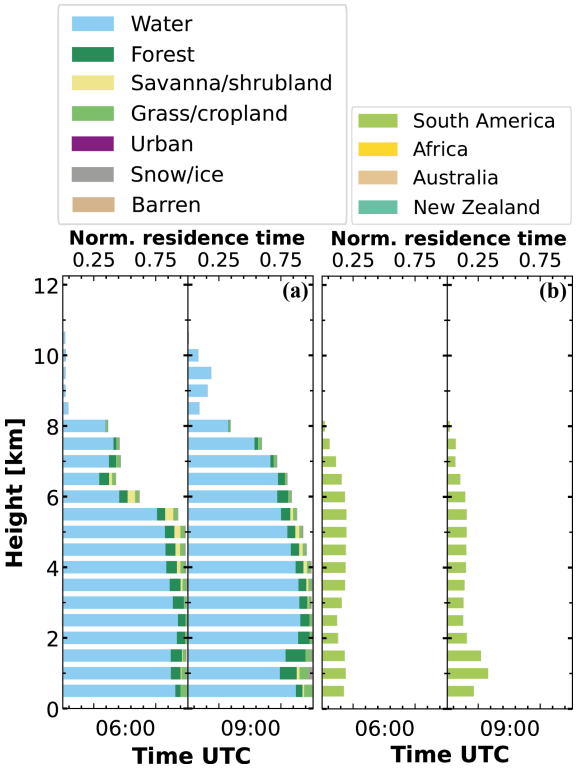

Figure 4. Normalized residence time as a function of height (km), and time (UTC) at which the air masses arrived at several heights over Punta Arenas on 5 February 2019. (**a**) Type of surface and (**b**) geographical regions. Residence time is calculated using a reception height of 8 km.

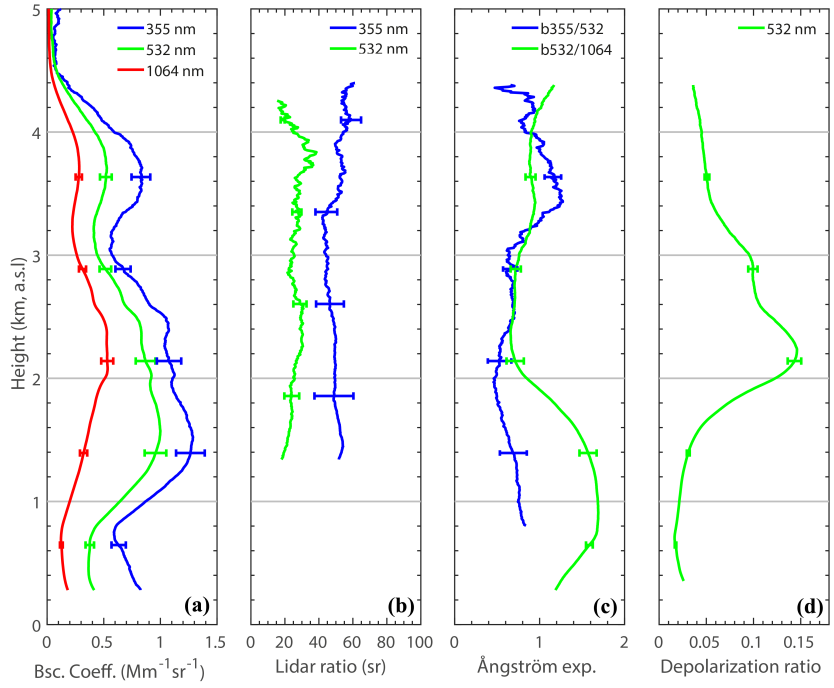

Figure 5. (**a**) Particle backscatter coefficients (at three wavelengths), (**b**) the extinction-to-backscatter ratios, (**c**) the corresponding backscatter-related Ångström exponents and (**d**) particle linear depolarization ratios measured at Punta Arenas on 5 February 2019, 07:51–08:57 UTC. Error bars depict the estimated uncertainties.

The potential impact of this event on cloud and precipitation evolution and life cycle can be investigated by means of CCN and INP concentrations. CCN and INP number concentrations have been derived for this plume (1–4.2 km), uncertainty range for this approach is of a factor of 2 and 3, respectively [22]. The lidar-derived total CCN concentration, given for 0.2% supersaturation with respect to liquid water, has a layer mean value and a standard deviation of 345 $\pm$ 77 cm^{-3}. The contribution of dust to the total CCN concentration is about 6% and the rest is attributed to soot particles. The obtained CCN number concentration is found to be strongly increased compared to other values reported for this region. Hamilton et al. [42] reported much lower monthly mean values of CCN concentration for January (50 to 100 cm^{-3}). For comparison, Schmale et al. [43] reported mean CCN concentrations within the range of 1200 to 1500 cm^{-3} (at 0.2% water supersaturation) for central Europe. We can therefore conclude that the CCN concentration was significantly increased due to the advection of smoke/dust, but was still below the levels typically observed in Central Europe. The parameterizations used for the derivation of the INP number concentration [23] correspond to soot particles in the immersion freezing temperature regime (see Figure 2f). From the lidar observations, a layer mean of 145 $\pm$ 75 INP per L (at -20 °C) was derived. This value corresponds only to soot particles since the contribution of dust particles to the total INP number concentration at the chosen temperature is weak and almost negligible. The INP number concentration is found to be elevated for the Southern Hemisphere, especially when compared with the typical values of the region (annual 1–5 $\times$ 10^{-3} INP/L for an activation temperature of -15 °C), where marine aerosol is the dominant aerosol type of INPs [44].

3.2. Long-Range Transported Smoke Layers from Australia

The next event of lofted aerosol layers that occurred during the DACAPO-PESO campaign was observed about one month after the previous layers (Section 3.1), on 11 March 2019. The temporal evolution of the event, by means of basic lidar parameters, aerosol target classification, AOD and thermodynamic profiles, is depicted in Figure 6. The AOD during that day was low, with a daily mean of 0.03 (500 nm). The layers were observed between 02:00 and 13:00 UTC and between 5 and 12 km altitude. In contrast with the observations from 5 February 2019, where the layer was located between 1.0 and 4.2 km in height, these layers were geometrically thin (approximately 1 km), and are located at considerably higher altitudes (see Figure 6b,d) but stacked upon each other. The backscatter coefficient values vary within the three layers, with the maximum being observed for the highest layer, which was observed at around 11–12 km height (Figure 6b). The highest layer can be separated from the other layers in terms of depolarization ratio as it is the only one that consists of particles causing depolarization (Figure 6c). Due to the low particle concentration and the uncertainties induced by the high altitude of the layers (decreasing signal-to-noise ratio with height), the target classification algorithm could not assign a specific aerosol type to the particles observed within the layer (Figure 6d). Apart from these high altitude layers, we also observed clouds, mostly confined in the lowest 2 km. Thus, in this specific case, we have no evidence that the aerosol did influence cloud formation, but nevertheless the particles may have the potential to do so if atmospheric conditions change.

This observed stratification of the multiple aerosol layers is a characteristic feature of plumes advected over transcontinental scales [39]. The long-range transport can be confirmed based on the back-trajectory analyses that are presented in Figures 7 and 8. As indicated by the 10-day HYSPLIT backward trajectories (Figures 7 and 8b), all the air parcels arriving at Punta Arenas on 11 March 2019, at 06:00 UTC and at 11 km altitude, originate from the southwestern coast of Australia and travelled at high altitudes above 10 km (Figure 7a). Before crossing the South Pacific Ocean, the air masses (above 5.5 km) appear to have a significant residence time above lands characterized as savanna/shrub and slightly less time above regions of grass, crops and forests (Figure 8a). According to FIRMS, when the air masses where above the southern parts of Australia, Tasmania

and New Zealand (approximately 9 days before they were observed above Punta Arenas), there was a high count of active fires (not shown here) in all the aforementioned regions. Similarly to the previous case, there are no hygroscopicity effects on the particles within the observed layers, since the relative humidity (Figure 7b) of the air masses observed above Punta Arena was less than 25%. In addition, there was no washout of the carried particles via wet deposition since the modeled total precipitation was almost negligible (less than 1 mm, Figure 7c).

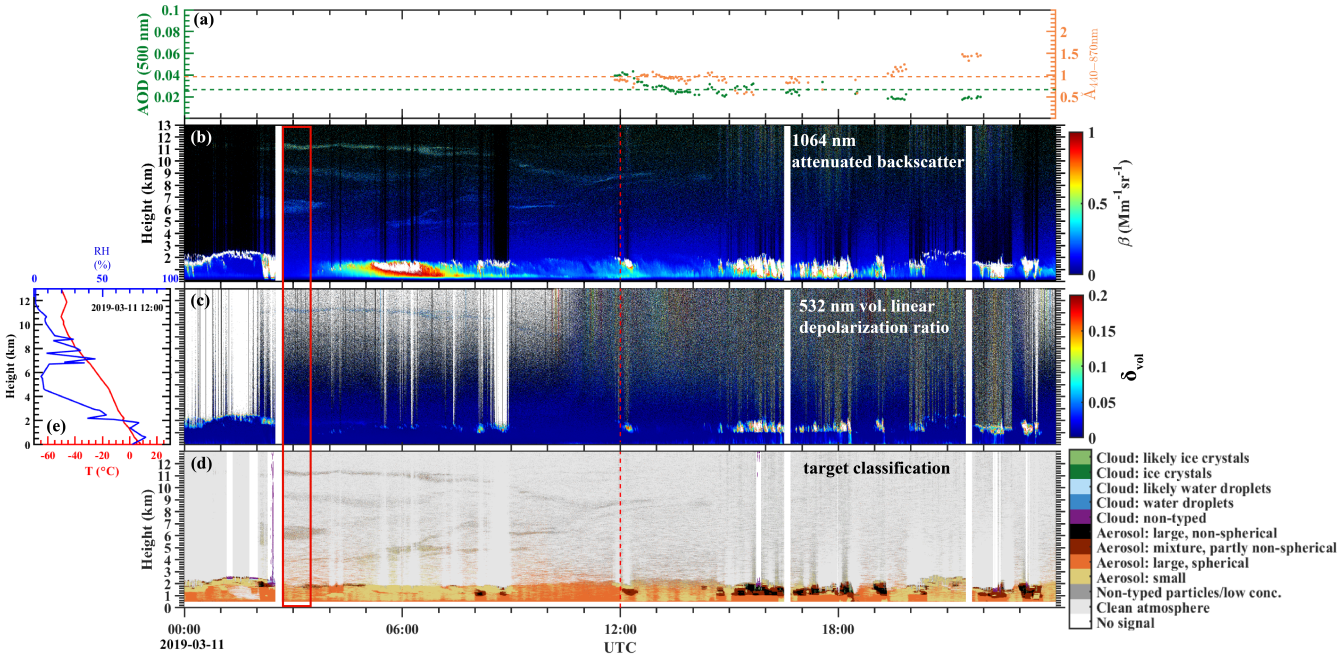

Figure 6. Sameas Figure 2 but for 11 March 2019. The averaging period for the profiles shown in Figure 9 is indicated by the red rectangul.

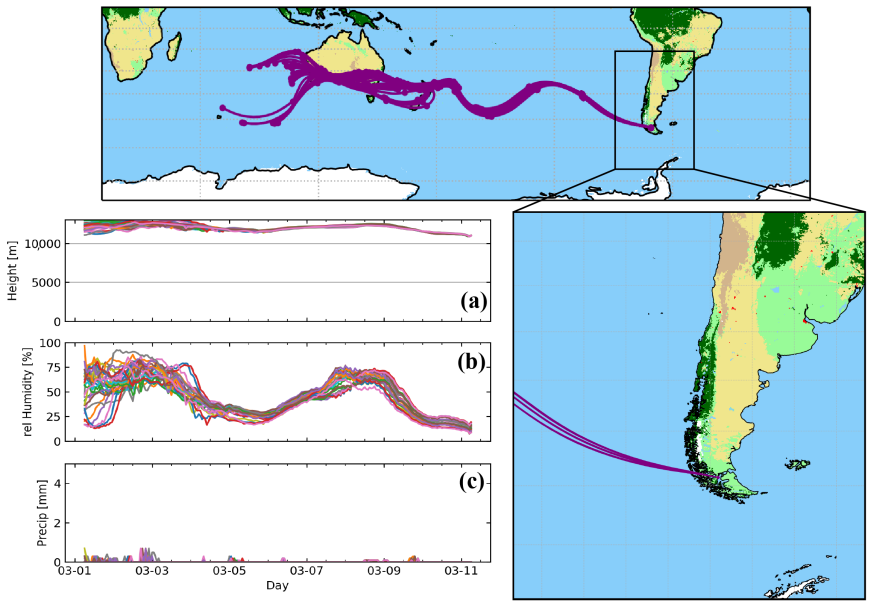

Figure 7. Same as Figure 3 but for 11 March 2019, 06:00 UTC, at 11 km altitude.

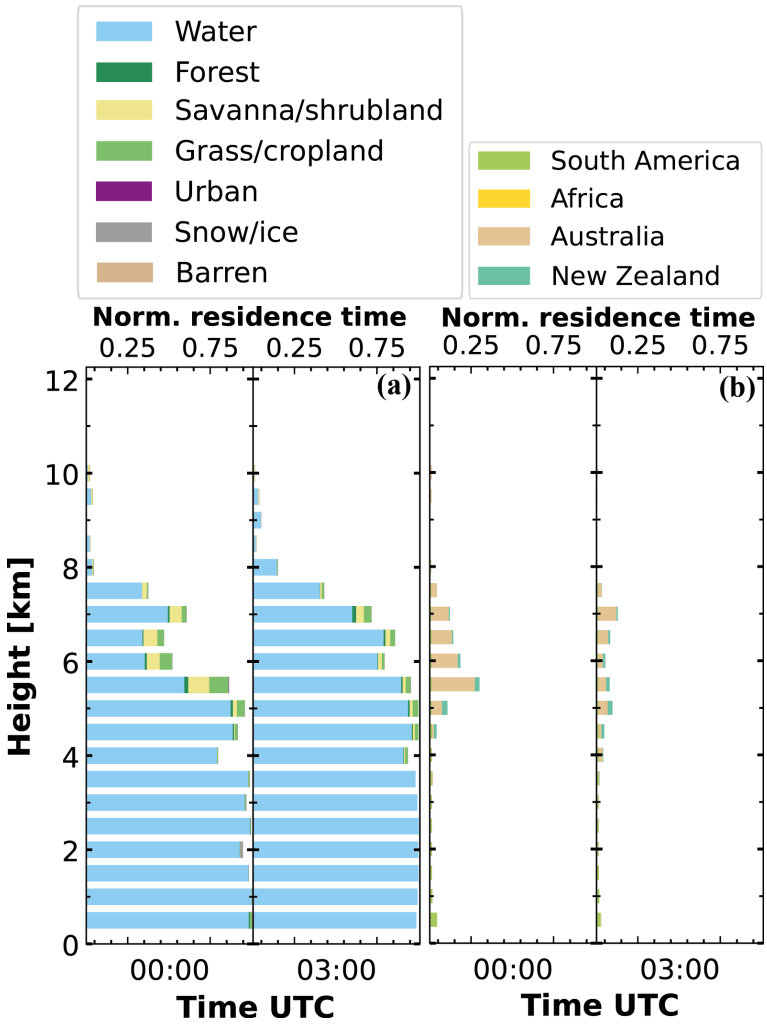

Figure 8. Same as Figure 4 but for 11 March 2019.

The height profiles of the backscatter coefficient, Ångström exponents and particle linear depolarization ratio as derived from the lidar measurements of 11 March 2019, between 2:45 and 3:40 UTC for the three lofted layers are shown in Figure 9. Profiles of extinction coefficient and lidar ratio are not presented due to low signal-to-noise ratio at the altitudes of interest. The three different layers are characterized by pronounced backscatter coefficients (Figure 9a). More specifically, the backscatter coefficient reached values up to 0.15 and 0.08 Mm^{-1} sr^{-1} for the layer located between 5.5 and 7.0 km; 0.09 and 0.06 Mm^{-1} sr^{-1} for the middle layer located around 9 km; and 0.35 and 0.18 Mm^{-1} sr^{-1} for the highest smoke layer observed around the altitude of 11 km (at 532 and 1064 nm respectively). The backscatter-related Ångström exponent (Figure 9b) at the wavelength pair of 532/1064 nm has a similar behavior for the lowest and highest layers with values up to 0.8, suggesting wavelength dependency and indicating the absence of coarse-mode aerosol particles. For the layer located at the altitude of 9 km, the Ångström exponent is considerably lower, with a mean of 0.22 $\pm$ 0.07, suggesting the presence of larger particles.

The particle linear depolarization ratio (Figure 9c) is height-independent up to 10 km with values of less than 2%. Similar values of particle linear depolarization ratio (<3%) have been reported by Baars et al. [45] for aged smoke in the Amazon rain forest during the dry season. Values of that range indicate that most of the particles observed are spherical in shape (i.e., smoke particles). More specifically, for the middle layer with the very low Ångström exponent values, we can conclude that most likely it consists of rather large, spherical particles of continental aerosol. Above 10 km high, we observed a sharp increase of the particle depolarization ratio, until it reached its maximum (9.5%) within

the highest aerosol layer, at an altitude of 11 km. Mean depolarization ratio values within this layer were 8.3 ± 1.02% at 532 nm. This increase of the depolarization ratio reveals that within the highest and driest (RH < 10%) layer there were irregularly shaped, partly coated soot particles. Dry, depolarizing smoke layers in the upper troposphere/lower stratosphere have been observed previously. Burton et al. [46] observed over Colorado, a similar smoke layer at a height of 8 km with a depolarization ratio of 9% at 532 nm. The increased depolarization ratio for dry smoke layers in the stratosphere was observed by Haarig et al. [37] and compared to more humid smoke layers in the lower troposphere with low values for the depolarization ratio (<5%). For an extensive literature overview on aged and fresh smoke properties based on multiwavelength lidar observations, readers may refer to [37].

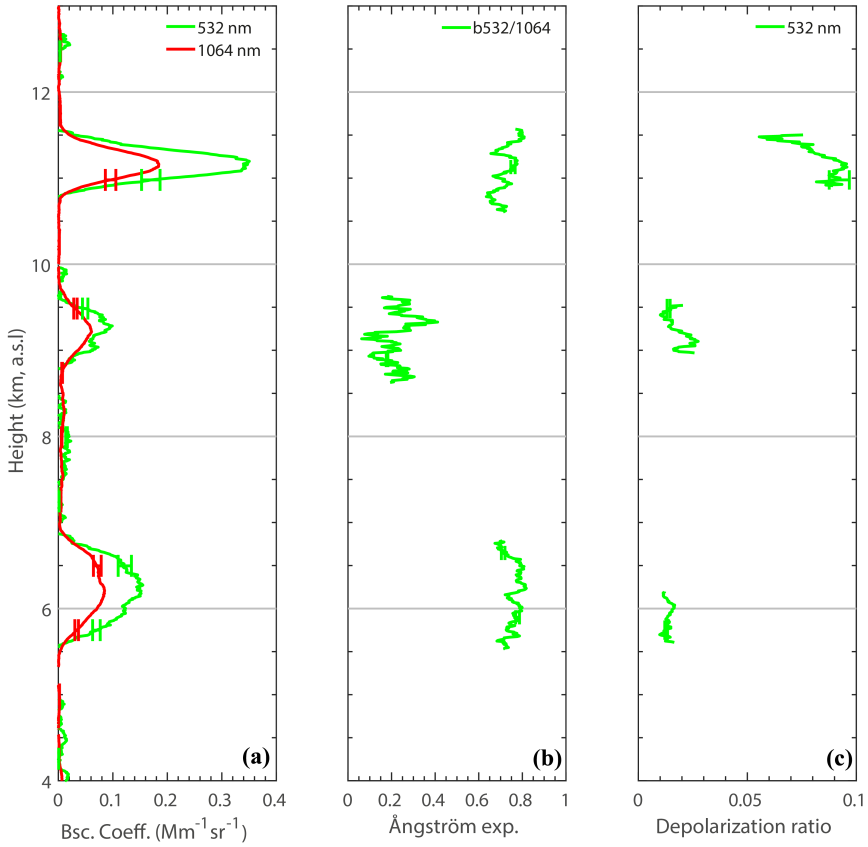

Figure 9. Mean profiles of (**a**) particle backscatter coefficients (at 532 and 1064 nm), (**b**) the corresponding backscatter-related Ångström exponents (for 532/1064 nm) and (**c**) particle linear depolarization ratios at 532 nm measured at Punta Arenas on 11 March 2019, 02:45–03:40 UTC. Error bars depict the estimated uncertainties.

INP number concentration was derived for the upper layer, which was observed around the altitude of 11 km. Since the temperature in the layer is below −35 °C (Figure 6e), the deposition nucleation freezing parameterization for soot of Ullrich et al. [23] is used. The whole backscatter coefficient was attributed to smoke particles, as the separation of dust and smoke does not work for smoke layers in the upper troposphere and lower stratosphere with their enhanced depolarization ratios. For an assumed supersaturation with respect to ice of 15%, an INP number concentration of 158 ± 105 L^{-1} was derived for ambient temperature. For the same superaturation and an assumed fixed temperature of −55 °C, the INP number concentration would be higher (167 ± 111 L^{-1}). Immersion freezing and CCN activation are not important at that temperature range. Based on satellite observations, a supersaturation with respect to ice of 15–20% is found to be the best choice in cirrus clouds in the northern midlattitudes [47]. The high numbers of smoke INP

observed at 11 km height will impact cirrus formation as soon as cooling or lifting of the air mass leads to an increase of relative humidity. Homogeneous ice formation will be suppressed, as it requires supersaturations of around 40% with respect to ice [48], while sufficient INP are present to form ice at much lower humidities.

3.3. Long-Term Analysis of Occurrence of Lofted Layers

Similarly to the ALPACA campaign [4,6], lofted aerosol layers in the troposphere were observed more frequently than expected in the pristine environment of Punta Arenas in 2019. Figure 10 gives an overview of the occurrence of lofted layers observed by the lidar (manually evaluated) in Punta Arenas from the beginning of the DACAPO-PESO campaign (27 November 2018) until 31 December 2019. In total, lofted aerosol layers were observed on 16 different days (3.9%). Most of the layers were both optically and geometrically thin. According to AERONET, the average daily mean AOD of the days, on which lofted aerosol layers occurred, was as low as 0.05 at 500 nm wavelength. In addition, almost all layers were non-depolarizing, indicating that they consisted mainly of spherical particles. The only exceptions were the layer presented in Section 3.1, and a thin layer that was observed on 3 December 2019 (slighlty depolarizing). Nevertheless, such layers have the potential to influence cloud formation in this environment which is supposed to be almost pristine. Even small perturbations could therefore influence cloud properties strongly, while in the polluted northern hemisphere such perturbations would not be observable. This notion is also corroborated by the study of Villanueva et al. [49], who discuss the hemispheric differences in the effect of mineral dust on heterogeneous ice formation.

10-day HYSPLIT backward trajectories for all the layers were performed, and revealed that the main origins of the air masses were the southern Oceans including Australia and New Zealand. To be more specific, layers observed until October 2019 originated mainly from the Southern Pacific and the Southern Ocean (and consisted of marine particles mostly), with only a fraction tracing back to the southern tips of Australia and South America (e.g., Section 3.1). Their origin and optical properties (not presented here), indicate that they were likely mainly consisting of large and spherical particles. The layers observed in November and December 2019 were originating mainly from Australia. Given the origin of the air masses, their altitude and geometrical as well as optical properties, the layers can be directly linked to the outstanding Australian bushfires of 2019–2020 [10].

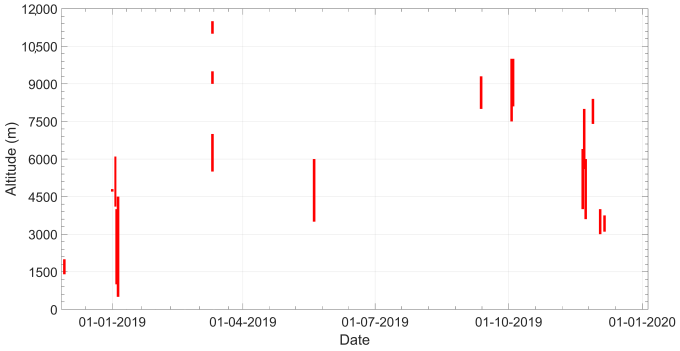

Figure 10. Occurrence and height boundaries of lofted aerosol layers in Punta Arenas between 27 November 2018 and 31 December 2019.

4. Conclusions

During the first 14 months of the DACAPO-PESO campaign, significant lofted layers were observed regularly above Punta Arenas. Two events were studied and presented in detail, based on observations from the multiwavelength Raman lidar Polly^{XT}. The Raman lidar observations in combination with the HYSPLIT backward trajectory analysis allowed the identification of the aerosol. In the first case, the lofted aerosol layers originated from Central and Central-South Chile, and were identified as smoke layers, mixed with soil

dust. Smoke and dust particles were probably mixed near the source and lofted to higher altitudes via convection. In the second case, several geometrically and optically thin smoke layers were observed, after long-range transport from Australia.

The differences in the obtained optical properties between the observed layers, reflect differences in the amount and the age (chemical composition) of the observed smoke particles. As it can be seen from Table 1, the 532-nm particle depolarization ratio for the smoke and soil dust mixtures is slightly lower than the one for the pure upper tropospheric smoke layer. In the first case, the smoke particles within the layer were freshly emitted (emitted 1–2 days before observation), while in the second case, the smoke particles were aged (observed 9 days after emission). Previous studies have shown that the depolarization ratio values at 532 nm for smoke freshly emitted into the atmosphere are generally low (due to the sphericity of the newly formed particles) and even lower for aged smoke particles (Haarig et al. [37], Burton et al. [46,50]). The elevated depolarization values of the smoke layer of the first case can additionally be attributed to the presence of soil dust and the resulting elevated mixing ratio of smoke and dust particles [51,52]. In addition, differences in RH are one of the main reasons for the different depolarization ratios. The backscatter-related Ångström exponent at the wavelength pair of 532/1064 nm exhibits similar behavior for both layers, with slightly higher values for the aged pure smoke layer, indicating a predominance of fine mode particles.

In comparison to the prevailing marine conditions in the region of Punta Arenas, biomass burning sources acted as an effective source of CCN and INP. Smoke advection from Central and Central-South Chile affected significantly the available CCN and INP in the lower troposphere. Both CCN and INP concentrations were higher than usual for the first case and likely contributed to the characteristics of an ice cloud that was observed only a couple of hours later (cloud formation, Figure 2d). In addition, smoke particles advected from Australia at high altitudes were found to likely facilitate the formation of ice crystals.

The Southern Oceans and more specifically Punta Arenas, are usually characterized as pristine environments, where clean marine aerosol conditions prevail. However, this study demonstrates that this is not always the case. Lofted aerosol layers, transported either from short or long distances, occur regularly and influence radiation and cloud formation processes above the region. Even small perturbations influence cloud properties strongly above Punta Arenas, but in the polluted northern hemisphere, such perturbations would not be observable.

Author Contributions: Conceptualization, A.A.; data curation, A.A.F., H.B., M.R., Z.Y. and M.H.; investigation, A.A.F.; methodology, A.A., U.W., H.B. and A.A.F., writing—original draft preparation, A.A.F.; writing—review and editing, A.A.F., H.B., M.R., M.H. and P.S.; resources, M.R., P.S., C.J., R.E., B.B. and F.Z. All authors have read and agreed to the published version of the manuscript.

Funding: Parts of the research leading to these results have received funding from the European Union's Horizon 2020 research and innovation programme under grant agreement number 654109(ACTRIS). The publication of this article was funded by the Open Access Fund of the Leibniz Association.

Acknowledgments: The Polly^{XT} lidar data are available at TROPOS upon request (polly@tropos.de). GDAS1 meteorological data are available and can be downloaded at the webpage of NOAA (https://ready.arl.noaa.gov/READYamet.php). AERONET sun-photometer data were downloaded from the AERONET web page (AERONET, 2019). Trajectories are calculated with the NOAA HYSPLIT model (HYSPLIT, 2019).

Conflicts of Interest: The authors declare no conflict of interest.

References

1. Schneider, C.; Glaser, M.; Kilian, R.; Santana, A.; Butorovic, N.; Casassa, G. Weather Observations Across the Southern Andes at 53°S. *Phys. Geogr.* **2003**, *24*, 119. [CrossRef]
2. Kanitz, T.; Seifert, P.; Ansmann, A.; Engelmann, R.; Althausen, D.; Casiccia, C.; Rohwer, E.G. Contrasting the impact of aerosols at northern and southern midlatitudes on heterogeneous ice formation. *Geophys. Res. Lett.* **2011**, *38*, 5. [CrossRef]

3. Kanitz, T.; Ansmann, A.; Foth, A.; Seifert, P.; Wandinger, U.; Engelmann, R.; Baars, H.; Althausen, D.; Casiccia, C.; Zamorano, F. Surface matters: Limitations of CALIPSO V3 aerosol typing in coastal regions. *Atmos. Meas. Tech.* **2014**, *7*, 2061–2072. [CrossRef]
4. Foth, A.; Kanitz, T.; Engelmann, R.; Baars, H.; Radenz, M.; Seifert, P.; Barja, B.; Fromm, M.; Kalesse, H.; Ansmann, A. Vertical aerosol distribution in the southern hemispheric midlatitudes as observed with lidar in Punta Arenas, Chile (53.2 degrees S and 70.9 degrees W), during ALPACA. *Atmos. Chem. Phys.* **2019**, *19*, 6217–6233. [CrossRef]
5. Immler, F.; Schrems, O. LIDAR measurements of cirrus clouds in the northern and southern midlatitudes during INCA (55°N, 53°S): A comparative study. *Geophys. Res. Lett.* **2002**, *29*, 56-1–56-4. [CrossRef]
6. Kanitz, T.; Ansmann, A.; Engelmann, R.; Althausen, D. North-south cross sections of the vertical aerosol distribution over the Atlantic Ocean from multiwavelength Raman/polarization lidar during Polarstern cruises. *J. Geophys. Res. Atmos.* **2013**, *118*, 2643–2655. [CrossRef] [PubMed]
7. Baars, H.; Kanitz, T.; Engelmann, R.; Althausen, D.; Heese, B.; Komppula, M.; Preissler, J.; Tesche, M.; Ansmann, A.; Wandinger, U.; et al. An overview of the first decade of Polly(NET): An emerging network of automated Raman-polarization lidars for continuous aerosol profiling. *Atmos. Chem. Phys.* **2016**, *16*, 5111–5137. [CrossRef]
8. Althausen, D.; Engelmann, R.; Baars, H.; Heese, B.; Ansmann, A.; Muller, D.; Komppula, M. Portable Raman Lidar Polly(XT) for Automated Profiling of Aerosol Backscatter, Extinction, and Depolarization. *J. Atmos. Ocean. Technol.* **2009**, *26*, 2366–2378. [CrossRef]
9. Engelmann, R.; Kanitz, T.; Baars, H.; Heese, B.; Althausen, D.; Skupin, A.; Wandinger, U.; Komppula, M.; Stachlewska, I.S.; Amiridis, V.; et al. The automated multiwavelength Raman polarization and water-vapor lidar Polly(XT): The neXT generation. *Atmos. Meas. Tech.* **2016**, *9*, 1767–1784. [CrossRef]
10. Ohneiser, K.; Ansmann, A.; Baars, H.; Seifert, P.; Barja, B.; Jimenez, C.; Radenz, M.; Teisseire, A.; Floutsi, A.; Haarig, M.; et al. Smoke of extreme Australian bushfires observed in the stratosphere over Punta Arenas, Chile, in January 2020: Optical thickness, lidar ratios, and depolarization ratios at 355 and 532 nm. *Atmos. Chem. Phys. Discuss.* **2020**, *20*, 8003–8015. [CrossRef]
11. Bühl, J.; Seifert, P.; Wandinger, U.; Baars, H.; Kanitz, T.; Schmidt, J.; Myagkov, A.; Engelmann, R.; Skupin, A.; Heese, B.; et al. LACROS: The Leipzig Aerosol and Cloud Remote Observations System. *SPIE Remote Sens.* **2013**, *8890*, 889002.
12. Holben, B.N.; Eck, T.F.; Slutsker, I.; Tanre, D.; Buis, J.P.; Setzer, A.; Vermote, E.; Reagan, J.A.; Kaufman, Y.J.; Nakajima, T.; et al. AERONET—A federated instrument network and data archive for aerosol characterization. *Remote Sens. Environ.* **1998**, *66*, 1–16. [CrossRef]
13. Ristori, P.; Otero, L.; Jin, Y.; Barja, B.; Shimizu, A.; Barbero, A.; Salvador, J.; Bali, J.L.; Herrera, M.; Etala, P.; et al. Saver.net lidar network in southern South America. *EPJ Web Conf.* **2018**, *176*, 09011. [CrossRef]
14. Ansmann, A.; Müller, D. Lidar and atmospheric aerosol particles. In *LIDAR: Range-Resolved Optical Remote Sensing of the Atmosphere*; Springer: New York, NY, USA, 2005; pp. 105–141.
15. Baars, H.; Ansmann, A.; Althausen, D.; Engelmann, R.; Heese, B.; Muller, D.; Artaxo, P.; Paixao, M.; Pauliquevis, T.; Souza, R. Aerosol profiling with lidar in the Amazon Basin during the wet and dry season. *J. Geophys. Res. Atmos.* **2012**, *117*, 16. [CrossRef]
16. Müller, D.; Ansmann, A.; Mattis, I.; Tesche, M.; Wandinger, U.; Althausen, D.; Pisani, G. Aerosol-type-dependent lidar ratios observed with Raman lidar. *J. Geophys. Res. Atmos.* **2007**, *112*. [CrossRef]
17. D'Amico, G.; Amodeo, A.; Baars, H.; Binietoglou, I.; Freudenthaler, V.; Mattis, I.; Wandinger, U.; Pappalardo, G. EARLINET Single Calculus Chain—Overview on methodology and strategy. *Atmos. Meas. Tech.* **2015**, *8*, 4891–4916. [CrossRef]
18. Mattis, I.; D'Amico, G.; Baars, H.; Amodeo, A.; Madonna, F.; Iarlori, M. EARLINET Single Calculus Chain—Technical—Part 2: Calculation of optical products. *Atmos. Meas. Tech.* **2016**, *9*, 3009–3029. [CrossRef]
19. Wandinger, U.; Freudenthaler, V.; Baars, H.; Amodeo, A.; Engelmann, R.; Mattis, I.; Gross, S.; Pappalardo, G.; Giunta, A.; D'Amico, G.; et al. EARLINET instrument intercomparison campaigns: Overview on strategy and results. *Atmos. Meas. Tech.* **2016**, *9*, 1001–1023. [CrossRef]
20. Freudenthaler, V. About the effects of polarising optics on lidar signals and the Delta 90 calibration. *Atmos. Meas. Tech.* **2016**, *9*, 4181–4255. [CrossRef]
21. Belegante, L.; Bravo-Aranda, J.A.; Freudenthaler, V.; Nicolae, D.; Nemuc, A.; Ene, D.; Alados-Arboledas, L.; Amodeo, A.; Pappalardo, G.; D'Amico, G.; et al. Experimental techniques for the calibration of lidar depolarization channels in EARLINET. *Atmos. Meas. Tech.* **2018**, *11*, 1119–1141. [CrossRef]
22. Mamouri, R.E.; Ansmann, A. Potential of polarization lidar to provide profiles of CCN- and INP-relevant aerosol parameters. *Atmos. Chem. Phys.* **2016**, *16*, 5905–5931. [CrossRef]
23. Ullrich, R.; Hoose, C.; Mohler, O.; Niemand, M.; Wagner, R.; Hohler, K.; Hiranuma, N.; Saathoff, H.; Leisner, T. A New Ice Nucleation Active Site Parameterization for Desert Dust and Soot. *J. Atmos. Sci.* **2017**, *74*, 699–717. [CrossRef]
24. Tesche, M.; Ansmann, A.; Muller, D.; Althausen, D.; Engelmann, R.; Freudenthaler, V.; Gross, S. Vertically resolved separation of dust and smoke over Cape Verde using multiwavelength Raman and polarization lidars during Saharan Mineral Dust Experiment 2008. *J. Geophys. Res. Atmos.* **2009b**, *114*, 14. [CrossRef]
25. Ansmann, A.; Ohneiser, K.; Mamouri, R.E.; Knopf, D.A.; Veselovskii, I.; Baars, H.; Engelmann, R.; Foth, A.; Jimenez, C.; Seifert, P.; et al. Tropospheric and stratospheric wildfire smoke profiling with lidar: Mass, surface area, CCN and INP retrieval. *Atmos. Chem. Phys. Discuss.* **2020**, *2020*, 1–45. [CrossRef]

26. Ansmann, A.; Mamouri, R.E.; Hofer, J.; Baars, H.; Althausen, D.; Abdullaev, S.F. Dust mass, cloud condensation nuclei, and ice-nucleating particle profiling with polarization lidar: Updated POLIPHON conversion factors from global AERONET analysis. *Atmos. Meas. Tech.* **2019**, *12*, 4849–4865. [CrossRef]
27. GDAS: Global Data Assimilation System, meteorological data base.
28. Holben, B.N.; Tanre, D.; Smirnov, A.; Eck, T.F.; Slutsker, I.; Abuhassan, N.; Newcomb, W.W.; Schafer, J.S.; Chatenet, B.; Lavenu, F.; et al. An emerging ground-based aerosol climatology: Aerosol optical depth from AERONET. *J. Geophys. Res. Atmos.* **2001**, *106*, 12067–12097. [CrossRef]
29. Stein, A.F.; Draxler, R.R.; Rolph, G.D.; Stunder, B.J.B.; Cohen, M.D.; Ngan, F. NOAA'S hysplit atmospheric transport and dispersion modeling system. *Bull. Am. Meteorol. Soc.* **2015**, *96*, 2059–2077. [CrossRef]
30. Radenz, M.; Seifert, P. Software for automated trajectory analysis: Trace, 2019. [CrossRef]
31. Radenz, M.; Seifert, P.; Baars, H.; Floutsi, A.A.; Yin, Z.; Bühl, J. Automated time-height-resolved airmass source attribution for profiling remote sensing applications. *Atmos. Chem. Phys. Discuss.* **2020**, *2020*, 1–21. [CrossRef]
32. Friedl, M.A.; McIver, D.K.; Hodges, J.C.F.; Zhang, X.Y.; Muchoney, D.; Strahler, A.H.; Woodcock, C.E.; Gopal, S.; Schneider, A.; Cooper, A.; et al. Global land cover mapping from MODIS: Algorithms and early results. *Remote Sens. Environ.* **2002**, *83*, 287–302. [CrossRef]
33. Baars, H.; Seifert, P.; Engelmann, R.; Wandinger, U. Target categorization of aerosol and clouds by continuous multiwavelength-polarization lidar measurements. *Atmos. Meas. Tech.* **2017**, *10*, 3175–3201. [CrossRef]
34. Nisantzi, A.; Mamouri, R.E.; Ansmann, A.; Hadjimitsis, D. Injection of mineral dust into the free troposphere during fire events observed with polarization lidar at Limassol, Cyprus. *Atmos. Chem. Phys.* **2014**, *14*, 12155–12165. [CrossRef]
35. Wagner, R.; Jahn, M.; Schepanski, K. Wildfires as a source of airborne mineral dust—Revisiting a conceptual model using large-eddy simulation (LES). *Atmos. Chem. Phys.* **2018**, *18*, 11863–11884. [CrossRef]
36. Amiridis, V.; Balis, D.S.; Giannakaki, E.; Stohl, A.; Kazadzis, S.; Koukouli, M.E.; Zanis, P. Optical characteristics of biomass burning aerosols over Southeastern Europe determined from UV-Raman lidar measurements. *Atmos. Chem. Phys.* **2009**, *9*, 2431–2440. [CrossRef]
37. Haarig, M.; Ansmann, A.; Baars, H.; Jimenez, C.; Veselovskii, I.; Engelmann, R.; Althausen, D. Depolarization and lidar ratios at 355, 532, and 1064 nm and microphysical properties of aged tropospheric and stratospheric Canadian wildfire smoke. *Atmos. Chem. Phys.* **2018**, *18*, 11847–11861. [CrossRef]
38. Balis, D.S.; Amiridis, V.; Zerefos, C.; Gerasopoulos, E.; Andreae, M.; Zanis, P.; Kazantzidis, A.; Kazadzis, S.; Papayannis, A. Raman lidar and sunphotometric measurements of aerosol optical properties over Thessaloniki, Greece during a biomass burning episode. *Atmos. Environ.* **2003**, *37*, 4529–4538. [CrossRef]
39. Müller, D.; Mattis, I.; Wandinger, U.; Ansmann, A.; Althausen, D.; Stohl, A. Raman lidar observations of aged Siberian and Canadian forest fire smoke in the free troposphere over Germany in 2003: Microphysical particle characterization. *J. Geophys. Res. Atmos.* **2005**, *110*, 16. [CrossRef]
40. Giannakaki, E.; Balis, D.S.; Amiridis, V.; Zerefos, C. Optical properties of different aerosol types: Seven years of combined Raman-elastic backscatter lidar measurements in Thessaloniki, Greece. *Atmos. Meas. Tech.* **2010**, *3*, 569–578. [CrossRef]
41. Tesche, M.; Gross, S.; Ansmann, A.; Muller, D.; Althausen, D.; Freudenthaler, V.; Esselborn, M. Profiling of Saharan dust and biomass-burning smoke with multiwavelength polarization Raman lidar at Cape Verde. *Tellus Ser. B Chem. Phys. Meteorol.* **2011**, *63*, 649–676. [CrossRef]
42. Hamilton, D.S.; Lee, L.A.; Pringle, K.J.; Reddington, C.L.; Spracklen, D.V.; Carslaw, K.S. Occurrence of pristine aerosol environments on a polluted planet. *Proc. Natl. Acad. Sci. USA* **2014**, *111*, 18466–18471. [CrossRef]
43. Schmale, J.; Henning, S.; Decesari, S.; Henzing, B.; Keskinen, H.; Sellegri, K.; Ovadnevaite, J.; Pohlker, M.L.; Brito, J.; Bougiatioti, A.; et al. Long-term cloud condensation nuclei number concentration, particle number size distribution and chemical composition measurements at regionally representative observatories. *Atmos. Chem. Phys.* **2018**, *18*, 2853–2881. [CrossRef]
44. Vergara-Temprado, J.; Murray, B.J.; Wilson, T.W.; O'Sullivan, D.; Browse, J.; Pringle, K.J.; Ardon-Dryer, K.; Bertram, A.K.; Burrows, S.M.; Ceburnis, D.; et al. Contribution of feldspar and marine organic aerosols to global ice nucleating particle concentrations. *Atmos. Chem. Phys.* **2017**, *17*, 3637–3658. [CrossRef]
45. Baars, H.; Ansmann, A.; Althausen, D.; Engelmann, R.; Artaxo, P.; Pauliquevis, T.; Souza, R. Further evidence for significant smoke transport from Africa to Amazonia. *Geophys. Res. Lett.* **2011**, *38*, 6. [CrossRef]
46. Burton, S.P.; Hair, J.W.; Kahnert, M.; Ferrare, R.A.; Hostetler, C.A.; Cook, A.L.; Harper, D.B.; Berkoff, T.A.; Seaman, S.T.; Collins, J.E.; et al. Observations of the spectral dependence of linear particle depolarization ratio of aerosols using NASA Langley airborne High Spectral Resolution Lidar. *Atmos. Chem. Phys.* **2015**, *15*, 13453–13473. [CrossRef]
47. Lamquin, N.; Stubenrauch, C.J.; Gierens, K.; Burkhardt, U.; Smit, H. A global climatology of upper-tropospheric ice supersaturation occurrence inferred from the Atmospheric Infrared Sounder calibrated by MOZAIC. *Atmos. Chem. Phys.* **2012**, *12*, 381–405. [CrossRef]
48. KÄrcher, B.; Jensen, E.J. Microscale characteristics of homogeneous freezing events in cirrus clouds. *Geophys. Res. Lett.* **2017**, *44*, 2027–2034. [CrossRef]
49. Villanueva, D.; Heinold, B.; Seifert, P.; Deneke, H.; Radenz, M.; Tegen, I. The day-to-day co-variability between mineral dust and cloud glaciation: A proxy for heterogeneous freezing. *Atmos. Chem. Phys.* **2020**, *20*, 2177–2199. [CrossRef]

50. Burton, S.P.; Ferrare, R.A.; Hostetler, C.A.; Hair, J.W.; Rogers, R.R.; Obland, M.D.; Butler, C.F.; Cook, A.L.; Harper, D.B.; Froyd, K.D. Aerosol classification using airborne High Spectral Resolution Lidar measurements—Methodology and examples. *Atmos. Meas. Tech.* **2012**, *5*, 73–98. [CrossRef]
51. Sugimoto, N.; Lee, C.H. Characteristics of dust aerosols inferred from lidar depolarization measurements at two wavelengths. *Appl. Opt.* **2006**, *45*, 7468–7474. [CrossRef]
52. Tesche, M.; Ansmann, A.; Muller, D.; Althausen, D.; Mattis, I.; Heese, B.; Freudenthaler, V.; Wiegner, M.; Esselborn, M.; Pisani, G.; et al. Vertical profiling of Saharan dust with Raman lidars and airborne HSRL in southern Morocco during SAMUM. *Tellus Ser. B Chem. Phys. Meteorol.* **2009**, *61*, 144–164. [CrossRef]